Frontiers of Information Technology & Electronic Engineering
www.jzus.zju.edu.cn; engineering.cae.cn; www.springerlink.com
ISSN 2095-9184 (print); ISSN 2095-9230 (online)
E-mail: jzus@zju.edu.cn

Correspondence:

Wideband circular-polarized transmitarray for generating a high-purity vortex beam*

Liangjie QIU[1,2,3,4], Xiuping LI[†‡1,2,3,4], Zihang QI[1,2,3,4], Wenyu ZHAO[1,2,3,4], Yuhan HUANG[5]

[1]*State Key Laboratory of Information Photonics and Optical Communications, Beijing 100876, China*

[2]*MOE Key Laboratory of Universal Wireless Communications, Beijing 100876, China*

[3]*Beijing Key Laboratory of Work Safety Intelligent Monitoring, Beijing 100876, China*

[4]*School of Electronic Engineering, Beijing University of Posts and Telecommunications, Beijing 100876, China*

[5]*Beijing Institute of Spacecraft System Engineering, Beijing 100094, China*

[†]E-mail: xpli@bupt.edu.cn

Received Nov. 3, 2022; Revision accepted Mar. 16, 2023; Crosschecked Apr. 27, 2023

https://doi.org/10.1631/FITEE.2200539

In this correspondence, a wideband circular-polarized (CP) transmitarray (TA) in the Ka-band is presented for generating a high-purity vortex beam. The proposed element is composed of two identical combinations separated by an air layer. The subwavelength structure and double-resonance characteristics ensure the stable phase shift of the element within the 1-dB transmission bandwidth of 28.4%. A square aperture TA fed by a horn antenna is fabricated and measured. Owing to the honeycomb arrangement of elements, the mode purity of $l=-1$ is >0.93 in a wide band from 28.5 to 38 GHz. The measured peak gain is 22.3 dBic, and the 3-dB axial ratio bandwidth is 27.6%. The performance of the proposed antenna demonstrates its potential for high-capacity wireless communication and high-quality radar imaging.

1 Introduction

With the development of wireless communication, the demand for wider bandwidth and higher data rates has significantly increased. The vortex beam carrying orbital angular momentum (OAM) is helically distributed, and was first proved in the field of optics (Allen et al., 1992). Theoretically, different OAM modes are orthogonal to each other, which enables multichannel wireless communication (Tamburini et al., 2012; Yan et al., 2014) and high-resolution radar imaging (Liu K et al., 2015; Liu HY et al., 2020).

Various approaches for generating vortex beams in microwave fields have been reported, including the patch antenna, uniform circular array, metasurface, and so on. The OAM patch antenna operating in high-order mode is good at obtaining high-purity characteristics. Nevertheless, the single-feed patch antenna (Li et al., 2020) faces the shortcomings of low gain and narrow bandwidth, whereas the feed network of the multiple-feed patch (Huang YH et al., 2019) is complex. A uniform circular array is a conventional method for generating vortex beams. However, the limited space between the elements dramatically increases the complexity of the feed network,

‡ Corresponding author

* Project supported by the National Natural Science Foundation of China (No. 61971051)

ORCID: Liangjie QIU, https://orcid.org/0009-0004-2820-4221; Xiuping LI, https://orcid.org/0000-0003-4350-9651

especially for high-purity vortex beams (Ma et al., 2021). In contrast to the above antennas, the OAM metasurface is fed by other source antennas and relies on adjusting the phase of each element. Thus, the metasurface has several advantages including simple feed and high degree of design freedom.

The metasurface falls into two main classifications, i.e., reflectarray (RA) and TA. In comparison to RA, the effect of feed-blockage is reduced in TA (Wu Z et al., 2005). So far, many TA elements have been proposed (Jiang et al., 2018; Ran et al., 2020; Veljovic and Skrivervik, 2020; Zhang FH et al., 2020; Zhang XL et al., 2020; Shahmirzadi et al., 2021). In Ran et al. (2020), the 1-dB transmission bandwidth was 25%, but the high profile was not suitable for wireless communication systems. In Jiang et al. (2018), Zhang FH et al. (2020), and Zhang XL et al. (2020), the elements consisted of fewer dielectric layers, but the transmission loss was >1 dB within the operating band. In Veljovic and Skrivervik (2020) and Shahmirzadi et al. (2021), the element achieved a low profile and high transmission simultaneously, but the 1-dB transmission bandwidth was <7% and limited the TA's bandwidth.

To generate the desired vortex beam, the phase shift of the element should meet the 360° requirement. So far, there are two main phase modulation methods commonly used in TA elements, i.e., the size-varying method (Akram MR et al., 2019) and the element rotation method (Zhang FH et al., 2019). The latter method is based on the Pancharatnam–Berry phase mechanism, which is also used to generate optical OAM beams (Wang et al., 2020; Wu YH et al., 2022). Notably, phase curve linearity is key to generating high-purity vortex beams. de Cos et al. (2011) revealed that the hexagonal element is smaller than the square element under the same operating bandwidth, and the phase linearity is also better. Huang YH et al. (2021) also verified this performance on size-varying elements. In addition, using the subwavelength element (Zhang FH et al., 2019) instead of the conventional half-wavelength or larger element (Bi et al., 2018; Lin et al., 2020; Wu GB et al., 2020) is beneficial for mode purity. In Huang HF and Li (2019), the period of elements was $0.38\lambda_0$ (λ_0 is the free-space wavelength at the center frequency), and the mode purity achieved 0.93 at the center frequency. Unfortunately, although the element was quarter wavelength (Akram Z et al., 2019), the mode purity suffered a significant decrease from 0.96 at the center frequency to 0.72 at the edge of the operating band. So, maintaining high purity in a wide band is still challenging.

The objective of this correspondence is to propose a wideband TA element for generating a high-purity vortex beam. The TA element achieves a good balance between the bandwidth and profile. The subwavelength elements are arranged in a honeycomb shape to provide more accurate phase compensation, thereby obtaining higher mode purity. As proof of the theoretical analysis, a CP TA in the Ka-band is fabricated and measured.

2 Wideband circular-polarized element design

2.1 Element rotation principle

The element rotation principle is based on the Pancharatnam–Berry phase mechanism. Assume that there is a left-handed circularly polarized (LHCP) wave traveling in the $+z$-direction illuminating the element, and that the CP transmission and reflection coefficients are expressed as (Xu et al., 2017; Akram MR et al., 2020)

$$t_{\mathrm{LR}}=\frac{1}{2}[(t_{xx}-t_{yy})-\mathrm{j}(t_{xy}+t_{yx})]\mathrm{e}^{-\mathrm{j}2\psi}, \tag{1}$$

$$r_{\mathrm{LL}}=\frac{1}{2}[(r_{xx}-r_{yy})-\mathrm{j}(r_{xy}+r_{yx})]\mathrm{e}^{-\mathrm{j}2\psi}, \tag{2}$$

$$t_{\mathrm{LL}}=\frac{1}{2}[(t_{xx}+t_{yy})-\mathrm{j}(t_{xy}-t_{yx})], \tag{3}$$

$$r_{\mathrm{LR}}=\frac{1}{2}[(r_{xx}+r_{yy})-\mathrm{j}(r_{xy}-r_{yx})], \tag{4}$$

where "L" and "R" stand for LHCP and right-handed circularly polarized (RHCP) waves respectively, ψ is the azimuthal rotation angle of the element, t_{LR} is the transmission coefficient from the LHCP wave to the RHCP wave, r_{LL} is the reflection coefficient from the LHCP wave to the LHCP wave, t_{LL} is the transmission coefficient from the LHCP wave to the LHCP wave, and r_{LR} is the reflection coefficient from the LHCP wave to the RHCP wave. Because there is a polarization conversion in the transmission process, the co-polarization of the transmitted wave is RHCP. As can be seen from Eq. (1), when rotating the element in the same direction, the phase of t_{LR} is twice of the rotation angle ψ. The expressions for the linearly transmitted and reflected waves in relation to

the linear-polarized component of the incident wave can be described as

$$\begin{bmatrix} E_{\mathrm{t}x} \\ E_{\mathrm{t}y} \end{bmatrix} = \begin{bmatrix} t_{xx} & t_{yx} \\ t_{xy} & t_{yy} \end{bmatrix} \begin{bmatrix} E_{\mathrm{i}x} \\ E_{\mathrm{i}y} \end{bmatrix},$$

$$\begin{bmatrix} E_{\mathrm{r}x} \\ E_{\mathrm{r}y} \end{bmatrix} = \begin{bmatrix} r_{xx} & r_{yx} \\ r_{xy} & r_{yy} \end{bmatrix} \begin{bmatrix} E_{\mathrm{i}x} \\ E_{\mathrm{i}y} \end{bmatrix},$$

where x and y are linear polarizations, $\boldsymbol{E}_{\mathrm{t}}$ and $\boldsymbol{E}_{\mathrm{r}}$ are the vectors representing the transmitted and reflected waves respectively, and $\boldsymbol{E}_{\mathrm{i}}$ is the vector of the incident wave.

2.2 Configuration and performance

The geometry of the TA element is shown in Fig. 1. The TA element consists of two identical combinations separated by an air layer. A combined metal layer form comtains an X-shaped patch, a hexagonal patch etched cross slot, and a rectangular patch. All of the dielectric layers use F_4BM220 (dielectric constant ε_{r}=2.2, loss tangent $\tan\delta$=0.001) with a thickness of H_2=0.5 mm. The period of the element is 3.6 mm (corresponding to $0.40\lambda_0$, where λ_0 is the free-space wavelength at 33.5 GHz). To achieve a wide band and a phase shift curve with good linearity, the influence of structure parameters on the transmission coefficient is investigated, as shown in Fig. 2. Finally, the angle θ of the X-shaped patch is 35°. Other detailed parameters are set as follows (unit: mm): L_1=2.5, L_2=2.5, L_3=2.9, L_4=2.7, W_1=0.7, W_2=1.5, H_1=0.5. In addition, the proposed element has a relatively low profile and the total thickness of the element is only 2.5 mm (corresponding to $0.28\lambda_0$).

The magnitudes of transmission and reflection coefficients are shown in Fig. 3. It can be seen that the magnitude of t_{LR} is maintained above −1 dB from 29 to 38.5 GHz. Within this frequency range, the magnitude of the cross-polarized transmission coefficient is below −15 dB, indicating the high

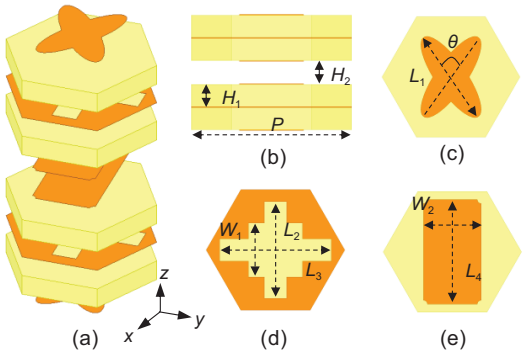

Fig. 1 Geometry of the proposed transmitarray (TA) element: (a) exploded view; (b) front view; (c) top view of the X-shaped patch; (d) top view of the hexagonal patch; (e) top view of the rectangular patch. Yellow denotes the dielectric layers and orange denotes the metal layers. References to color refer to the online version of this figure

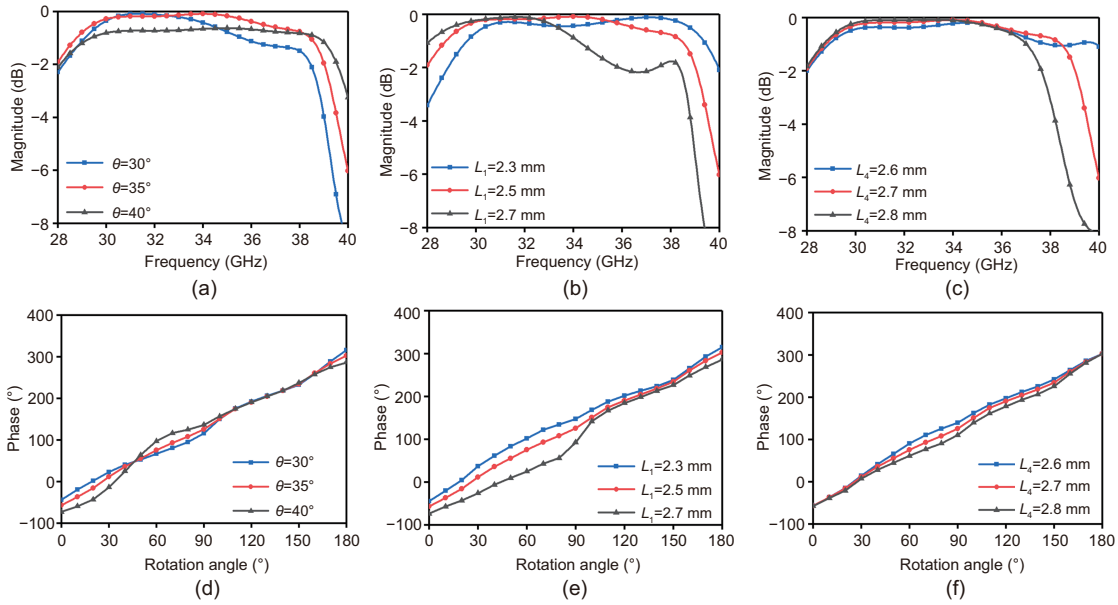

Fig. 2 Magnitude and phase of co-polarized transmission coefficients versus frequency and rotation angle with different θ (a, d), L_1 (b, e), and L_4 (c, f)

purity of the handedness-preserved CP transmission. Moreover, the magnitude of the reflection coefficient is below −10 dB, which avoids a high back lobe level. Based on these results and the comparison from Table 1, it follows that the proposed element achieves a good balance between low profile and wide band.

The stability of the transmitted phase shift is also an important index and affects the phase compensation accuracy of TA. From Fig. 4a, a full 360° phase range can be covered in a wide band, and the magnitude of the co-polarized transmission coefficient is simultaneously higher than −1 dB. In addition, when the rotation angle is gradually increased from 0° to 180° with an interval of 30°, the corresponding transmission phase responses are approximately double of the rotation angles, which agrees with the aforementioned theory. As shown in Fig. 4b, when the oblique incidence angle is <30°, the phase curve is almost linear and the high transmission is maintained in the rotation process. Comparing Fig. 4a with Fig. 4c, the phase linearity of the honeycomb element is significantly better than that of the square element.

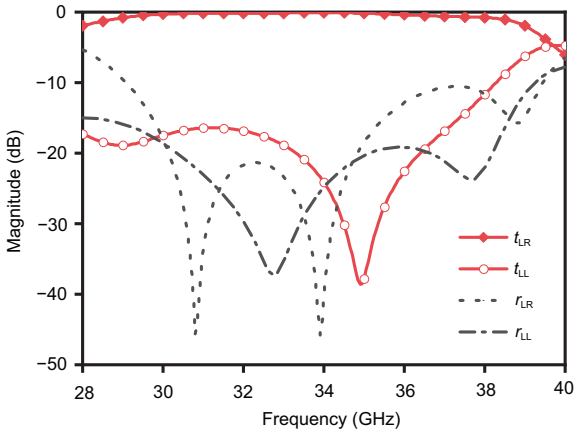

Fig. 3 Magnitude of transmission and reflection coefficients versus frequency under the normal incidence

3 Vortex beam transmitarray design

Based on the phase characteristics of a vortex beam carrying OAM (Allen et al., 1992), the required phase shift Ψ_{mn} of each element for the desired beam can be determined as

$$\Psi_{mn} = k_0 \cdot (|\boldsymbol{r}_{mn} - \boldsymbol{r}_{\mathrm{f}}| - \boldsymbol{r}_{mn} \cdot \boldsymbol{u}) + l \cdot \arctan\frac{Y_{mn}}{X_{mn}}, \quad (5)$$

where k_0 is the wave number in the free space corresponding to the operating frequency, $\boldsymbol{r}_{mn}$ is the position vector of the element on the m^{th} row and n^{th} column, $\boldsymbol{r}_{\mathrm{f}}$ is the vector from the phase center of the feed to the TA's center, $\boldsymbol{u}$ is the direction vector of the desired beam, l represents the OAM mode, and (X_{mn}, Y_{mn}) is the coordinate of the element on the m^{th} row and n^{th} column on the beam's normal plane.

The influence of the arrangement method on OAM mode purity is analyzed. Based on the phase compensation in Eq. (5), two square aperture TAs arranged in square and honeycomb shapes are designed separately. The OAM mode purity is calculated using the numerical Fourier transform of the aperture phase function. The relationship between the OAM spectrum A_{l_n} and the sampling phase $\Psi(\psi)$ is given by Yao et al. (2006) as follows:

$$A_{l_n} = \frac{1}{2\pi}\int_0^{2\pi} \Psi(\psi) \mathrm{e}^{-\mathrm{j}l_n\psi} \mathrm{d}\psi, \quad (6)$$

$$\text{Mode purity} = \frac{|A_{l_n}|}{\sum_{m=-\infty}^{+\infty} |A_{l_m}|}. \quad (7)$$

As shown in Fig. 5 and Table 2, when the effective radiation areas are both $10\lambda_0 \times 10\lambda_0$ and the periods

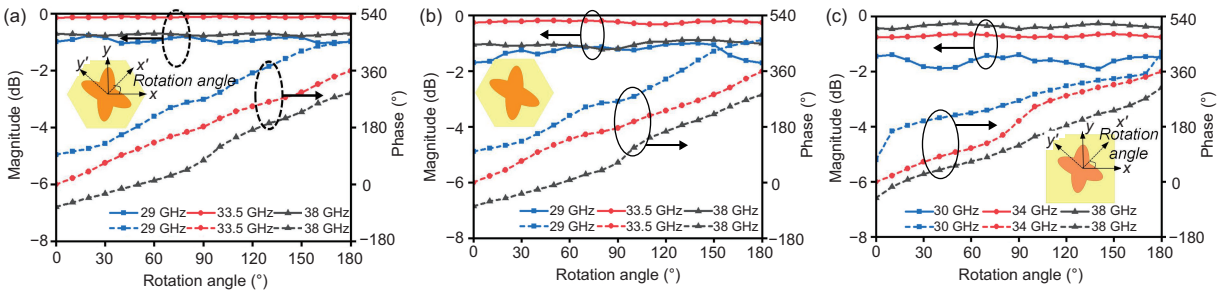

Fig. 4 Magnitude and phase of co-polarized transmission coefficient versus rotation angle of the element at different frequencies: (a) under normal incidence; (b) oblique incidence angle=30°; (c) under normal incidence

Table 1 Comparison with other reported transmitarray (TA) elements based on the element rotation principle

Reference	f_0 (GHz)	Number of dielectric layers	Profile ($\times\lambda_0$)	Transmission bandwidth*
Shahmirzadi et al. (2021)	34	2	0.18	3.5% (>−1 dB)
Veljovic and Skrivervik (2020)	24.6	2	0.13	6.0% (>−1 dB)
Jiang et al. (2018)	30	2	0.31	9.1% (>−1.9 dB)
Zhang XL et al. (2020)	20	2	0.21	10.0% (>−2.7 dB)
Zhang FH et al. (2020)	10	3	0.14	17.5% (>−3 dB)
Ran et al. (2020)	15	4	0.66	25.0% (>−1 dB)
This work	**33.5**	**4**	**0.28**	**28.4% (>−1 dB)**

* Transmission bandwidth is the frequency range in which the magnitude of the co-polarized transmission coefficient is greater than the value in brackets

Table 2 Comparison with other transmitarrays (TAs) based on different arrangement methods

Arrangement method	Number of elements	Mode purity	OAM bandwidth (%)
Square	625	>0.88	23.5
Honeycomb	**941**	**>0.93**	**28.4**

Aperture size: $10\lambda_0\times10\lambda_0$. OAM: orbital angular momentum

of the elements are both $0.4\lambda_0$, the honeycomb TA can accommodate more elements compared with the square TA. Moreover, the phase linearity of the honeycomb elements is better. Thus, the phase compensation accuracy is improved and higher mode purity is obtained.

Therefore, the honeycomb arrangement method is chosen. The effective radiation area of the honeycomb TA is 90 mm×90 mm. An LHCP horn antenna with a maximum gain of 15.2 dBic is used as a feeding source. The radiation pattern of the horn is approximately represented as a $\cos^{q_f}(\theta)$ function (feed pattern factor q_f=13.5), and the axial ratio is <3 dB in the whole Ka-band. To achieve a good trade-off between the spillover loss and the amplitude tapering across the TA, the F/D (focal-diameter ratio) is set as 1.0. Consequently, the maximum oblique incidence angle is 26.6°, and the proposed TA elements can be applied. The phase distribution for $l=-1$ is shown in Fig. 6a.

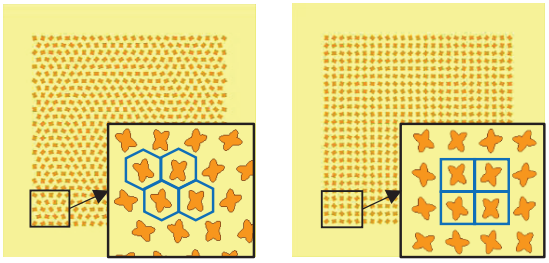

Fig. 5 Schematic of transmitarray (TA) using different arrangement methods: (a) honeycomb; (b) square

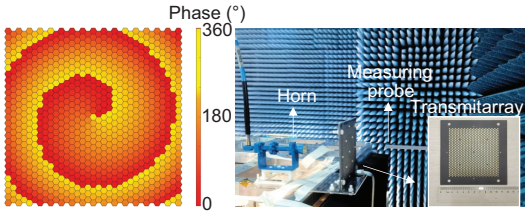

Fig. 6 Phase distribution of transmitarray (TA) (a) and configuration of the planar near-field measurement system (b)

4 Results and discussion

A TA for generating a vortex beam is simulated, fabricated, and measured by a planar near-field measurement system (Fig. 6b). A 90 mm×90 mm scanning plane is set 300 mm away from the TA with a measuring step of 5 mm. The simulation and measurement results in the near field are provided in Fig. 7. It is clear that the electric field (E-field) phase is a standard anticlockwise spiral with l=−1, and the magnitude has a central hole from 28.5 to 38 GHz. Moreover, as depicted in Fig. 8, the OAM mode purity of l=−1 is >0.93 in the range of 28.5–38 GHz, and is still high at the edge of the operating band, which illustrates the good quality of the generated vortex beam. In other words, the mode purity bandwidth is 28.4%.

The results of gain and axial ratio are plotted in Fig. 9. The measured peak gain of the proposed antenna is 22.3 dBic at 37.5 GHz and the 1-dB gain bandwidth is 17.1%. The 3-dB axial ratio bandwidth

is 27.6% from 28 to 37 GHz. A slight discrepancy between the simulation and measurement results is mainly due to the increase in the air gap between the dielectric layers caused by the fabrication tolerance.

The structural characteristics and performance of different OAM antennas are listed in Table 3. Compared with Bi et al. (2018), Lin et al. (2020), and Wu GB et al. (2020), the proposed TA using sub-wavelength elements achieves more accurate phase compensation and higher mode purity. Although the size of elements used in Zhang FH et al. (2019) is smaller, the proposed element arranged in the honeycomb shape shows more stable performance at the edge of the operating band. For this reason, the proposed TA has a wider bandwidth and higher mode purity compared with the antennas in Zhang FH et al. (2019).

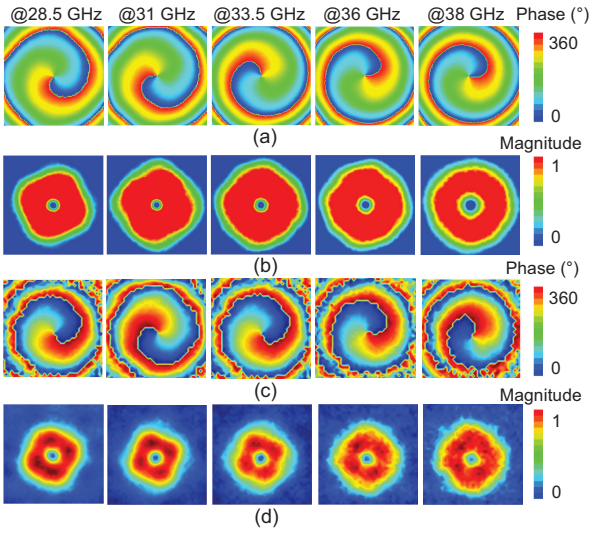

Fig. 7 Results of E-field phase and magnitude distributions in the near field for l=−1 at different frequencies: (a) simulated phase; (b) simulated magnitude; (c) measured phase; (d) measured magnitude

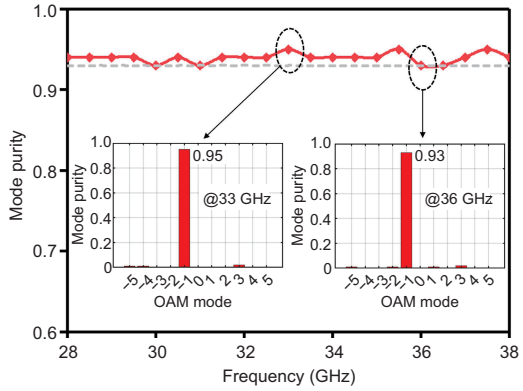

Fig. 8 Mode purity of the vortex beam versus frequency (OAM: orbital angular momentum)

5 Conclusions

This correspondence describes a wideband element and a TA for generating a high-purity vortex beam. As validated by fabrication and measurement, the radiated beam maintains typical vortex characteristics in a wide band from 28.5 to 38 GHz. Specifically, OAM mode purity is >0.93 within 28.4% mode purity bandwidth. Due to the wideband and high purity properties, the proposed TA antenna will find several applications, such as large-capacity wireless communication and high-quality radar imaging.

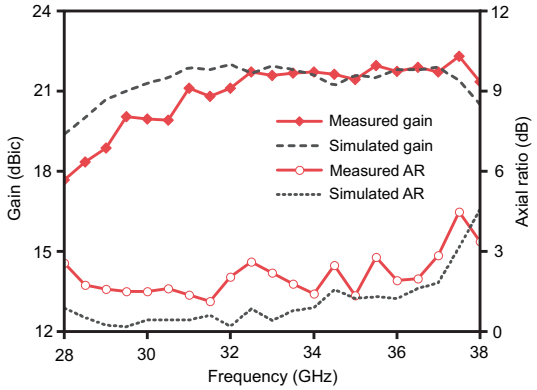

Fig. 9 Simulation and measurement results of gain and axial ratio (AR)

Table 3 Comparison with other reported orbital angular momentum (OAM) antennas

Reference	Type	f_0 (GHz)	Period of element ($\times\lambda_0$)	Aperture ($\times\lambda_0^2$)	Mode purity	Mode purity bandwidth (%)*
Zhang FH et al. (2019)	TA	10	0.33	5×5	>0.87	20.0
Bi et al. (2018)	RA	63	0.63	31×31	>0.79	17.1
Lin et al. (2020)	RA	23	0.77	15×15	>0.75	43.4
Wu GB et al. (2020)	TA	300	0.50	13×13	>0.40	31.3
This work	**TA**	**33.5**	**0.40**	**10×10**	**>0.93**	**28.4**

* Mode purity bandwidth refers to the frequency range in which the OAM mode purity is greater than the value of the previous column. TA: transmitarray; RA: reflectarray

Contributors

Liangjie QIU designed the research and performed the simulations. Liangjie QIU, Zihang QI, and Yuhan HUANG processed the data. Liangjie QIU drafted the paper. Xiuping LI and Wenyu ZHAO helped organize the paper. Liangjie QIU, Xiuping LI, Zihang QI, and Wenyu ZHAO revised and finalized the paper.

Acknowledgements

The authors would like to thank the Beijing Engineering Research Center of Electro Magnetic Compatibility (EMC) and Antenna Test Technology for the measurement support.

Compliance with ethics guidelines

Liangjie QIU, Xiuping LI, Zihang QI, Wenyu ZHAO, and Yuhan HUANG declare that they have no conflict of interest.

Data availability

The data that support the findings of this study are available from the corresponding author upon reasonable request.

References

Akram MR, Bai XD, Jin RH, et al., 2019. Photon spin hall effect-based ultra-thin transmissive metasurface for efficient generation of OAM waves. *IEEE Trans Antenn Propag*, 67(7):4650-4658. https://doi.org/10.1109/TAP.2019.2905777

Akram MR, Ding GW, Chen K, et al., 2020. Ultrathin single layer metasurfaces with ultra-wideband operation for both transmission and reflection. *Adv Mater*, 32(12):1907308. https://doi.org/10.1002/adma.201907308

Akram Z, Li XP, Qi ZH, et al., 2019. Wideband vortex beam reflectarray design using quarter-wavelength element. *IEEE Antenn Wirel Propag Lett*, 18(7):1458-1462. https://doi.org/10.1109/LAWP.2019.2919782

Allen L, Beijersbergen MW, Spreeuw RJC, et al., 1992. Orbital angular momentum of light and the transformation of Laguerre–Gaussian laser modes. *Phys Rev A*, 45(11):8185-8189. https://doi.org/10.1103/PhysRevA.45.8185

Bi F, Ba ZL, Wang X, 2018. Metasurface-based broadband orbital angular momentum generator in millimeter wave region. *Opt Expr*, 26(20):25693-25705. https://doi.org/10.1364/OE.26.025693

de Cos ME, Alvarez Y, Las-Heras F, 2011. Novel broadband artificial magnetic conductor with hexagonal unit cell. *IEEE Antenn Wirel Propag Lett*, 10:615-618. https://doi.org/10.1109/LAWP.2011.2159472

Huang HF, Li SN, 2019. High-efficiency planar reflectarray with small-size for OAM generation at microwave range. *IEEE Antenn Wirel Propag Lett*, 18(3):432-436. https://doi.org/10.1109/LAWP.2019.2893321

Huang YH, Li XP, Li QW, et al., 2019. Generation of broadband high-purity dual-mode OAM beams using a four-feed patch antenna: theory and implementation. *Sci Rep*, 9:12977. https://doi.org/10.1038/s41598-019-49377-6

Huang YH, Li XP, Akram Z, et al., 2021. Generation of millimeter-wave nondiffracting airy OAM beam using a single-layer hexagonal lattice reflectarray. *IEEE Antenn Wirel Propag Lett*, 20(6):1093-1097. https://doi.org/10.1109/LAWP.2021.3073144

Jiang ZH, Kang L, Hong W, et al., 2018. Highly efficient broadband multiplexed millimeter-wave vortices from metasurface-enabled transmit-arrays of subwavelength thickness. *Phys Rev Appl*, 9(6):064009. https://doi.org/10.1103/PhysRevApplied.9.064009

Li WW, Zhang L, Yang SY, et al., 2020. A reconfigurable second-order OAM patch antenna with simple structure. *IEEE Antenn Wirel Propag Lett*, 19(9):1531-1535. https://doi.org/10.1109/LAWP.2020.3008447

Lin ZS, Ba ZL, Wang X, 2020. Broadband high-efficiency electromagnetic orbital angular momentum beam generation based on a dielectric metasurface. *IEEE Photon J*, 12(3):4600611. https://doi.org/10.1109/JPHOT.2020.2991114

Liu HY, Liu K, Cheng YQ, et al., 2020. Microwave vortex imaging based on dual coupled OAM beams. *IEEE Sens J*, 20(2):806-815. https://doi.org/10.1109/JSEN.2019.2943698

Liu K, Cheng YQ, Yang ZC, et al., 2015. Orbital-angular-momentum-based electromagnetic vortex imaging. *IEEE Antenn Wirel Propag Lett*, 14:711-714. https://doi.org/10.1109/LAWP.2014.2376970

Ma JC, Song XY, Yao YC, et al., 2021. Research on the purity of orbital angular momentum beam generated by imperfect uniform circular array. *IEEE Antenn Wirel Propag Lett*, 20(6):968-972. https://doi.org/10.1109/LAWP.2021.3068287

Ran YZ, Cai T, Shi LH, et al., 2020. High-performance transmissive broadband vortex beam generator based on Pancharatnam–Berry metasurface. *IEEE Access*, 8:111802-111810. https://doi.org/10.1109/ACCESS.2020.3002547

Shahmirzadi AV, Badamchi Z, Badamchi B, et al., 2021. Generating concentrically embedded spatially divided OAM carrying vortex beams using transmitarrays. *IEEE Trans Antenn Propag*, 69(12):8436-8448. https://doi.org/10.1109/TAP.2021.3090860

Tamburini F, Mari E, Sponselli A, et al., 2012. Encoding many channels on the same frequency through radio vorticity: first experimental test. *New J Phys*, 14(3):033001. https://doi.org/10.1088/1367-2630/14/3/033001

Veljovic MJ, Skrivervik AK, 2020. Circularly polarized transmitarray antenna for cubesat intersatellite links in *K*-band. *IEEE Antenn Wirel Propag Lett*, 19(10):1749-1753. https://doi.org/10.1109/LAWP.2020.3016340

Wang B, Liu WZ, Zhao MX, et al., 2020. Generating optical vortex beams by momentum-space polarization vortices centred at bound states in the continuum. *Nat Photon*, 14(10):623-628. https://doi.org/10.1038/s41566-020-0658-1

Wu GB, Chan KF, Qu SW, et al., 2020. Orbital angular momentum (OAM) mode-reconfigurable discrete dielectric lens operating at 300 GHz. *IEEE Trans Terahertz Sci Technol*, 10(5):480-489. https://doi.org/10.1109/TTHZ.2020.2984451

Wu YH, Kang L, Werner DH, 2022. Active quasi-BIC optical vortex generators for ultrafast switching. *New J Phys*, 24(3):033002. https://doi.org/10.1088/1367-2630/ac52c0

Wu Z, Zhang WX, Liu ZG, et al., 2005. Reduction of feed blockage in reflectarray by orthogonally polarized transformation. IEEE Antennas and Propagation Society Int Symp, p.325-328. https://doi.org/10.1109/APS.2005.1552655

Xu HX, Liu HW, Ling XH, et al., 2017. Broadband vortex beam generation using multimode Pancharatnam–Berry metasurface. *IEEE Trans Antenn Propag*, 65(12):7378-7382. https://doi.org/10.1109/TAP.2017.2761548

Yan Y, Xie GD, Lavery MPJ, et al., 2014. High-capacity millimetre-wave communications with orbital angular momentum multiplexing. *Nat Commun*, 5:4876. https://doi.org/10.1038/ncomms5876

Yao E, Franke-Arnold S, Courtial J, et al., 2006. Fourier relationship between angular position and optical orbital angular momentum. *Opt Expr*, 14(20):9071-9076. https://doi.org/10.1364/OE.14.009071

Zhang FH, Song Q, Yang GM, et al., 2019. Generation of wideband vortex beam with different OAM modes using third-order meta-frequency selective surface. *Opt Expr*, 27(24):34864-34875. https://doi.org/10.1364/OE.27.034864

Zhang FH, Yang GM, Jin YQ, 2020. Low-profile circularly polarized transmitarray for wide-angle beam control with a third-order meta-FSS. *IEEE Trans Antenn Propag*, 68(5):3586-3597. https://doi.org/10.1109/TAP.2020.2964957

Zhang XL, Yang F, Xu SH, et al., 2020. Dual-layer transmitarray antenna with high transmission efficiency. *IEEE Trans Antenn Propag*, 68(8):6003-6012. https://doi.org/10.1109/TAP.2020.2989555